



# Effect of heat input on microstructure and mechanical property of wire-arc additive manufactured Ti-6Al-4V alloy

Guo Xian<sup>1</sup> · Jeong mok Oh<sup>2</sup> · Junghoon Lee<sup>3</sup> · Sang Myung Cho<sup>4</sup> · Jong-Tak Yeom<sup>2</sup> · Yoonsuk Choi<sup>1</sup> · Namhyun Kang<sup>1</sup>

Received: 10 August 2021 / Accepted: 29 December 2021 / Published online: 2 February 2022  
© International Institute of Welding 2022

## Abstract

Wire-arc additive manufacturing (WAAM) combines an electric arc as a heat source and a wire as feedstock to build a layer-by-layer component. In arc welding, heat input is an important characteristic because it influences the cooling rate, which can affect the mechanical properties and microstructure of the deposited material. We investigated the effect of heat input on the microstructure and mechanical properties of WAAM deposited Ti-6Al-4V alloys. A high heat input ( $10^6$  J/m, specimen H) produced a columnar grain exhibiting a large anisotropic tensile strength. However, a low heat input ( $5 \times 10^5$  J/m, specimen L) transformed the columnar grains to equiaxed grains owing to the accelerated solidification rates. The thermal history of the WAAM deposits was simulated using the finite-element method. The faster cooling rates in the solidification range (1600–1660 °C) in specimen L resulted in a larger fraction of the equiaxed grains and significant reduction of tensile strength anisotropy. Meanwhile, due to more thermal cycles and rapid cooling rates during the secondary- $\alpha$  transformation below the  $\beta$ -transus temperature (700–1006 °C), specimen H produced larger amounts of nitrogen,  $\alpha'$  martensite and fine-secondary  $\alpha$  with a tangled dislocation, thereby exhibiting a larger tensile strength and hardness than specimen L.

**Keywords** WAAM · Ti-6Al-4V · Heat input · Equiaxed grain · Thermal history · Secondary  $\alpha$

## 1 Introduction

The Ti-6Al-4V or Ti64 alloys have been widely commercialised in fields such as aerospace and chemical engineering, owing to their excellent physical properties. However, the high cost and inferior machinability of Ti64 alloys make it difficult to produce large-scale titanium alloy components, specifically with complex geometries. A low-cost

technology called wire-arc additive manufacturing (WAAM) has recently gained attention for its high deposition rate and high material utilisation [1–3]. Specifically, the GTAW-based WAAM is an environment-friendly producing less fume and spatter with a significant applicability using various electrode types and shapes [4]. In essence, layer deposition technology relies on gas tungsten arc welding (GTAW), which is similar to a multi-pass welding process [5–7].

WAAM is an economical alternative to conventional manufacturing methods, such as for cast and forged Ti64, and the properties of the components produced must match or surpass the properties of those produced through traditional approaches. The solidification of the arc welding process normally exhibits epitaxial growth from the adjacent melted substrate and tends to form columnar grain structures [8]. Along the build direction, the columnar prior- $\beta$  grains in additive manufacturing (AM)-fabricated Ti64 are characterised by a strong orientation, which contributes to anisotropic tensile elongation properties [9]; however, this is undesirable for the component. Therefore, the primary objective of metal AM is to minimise the variation in the mechanical properties in various directions by transforming the columnar prior- $\beta$  grains into equiaxed grains.

Recommended for publication by Commission IX—Behaviour of Metals Subjected to Welding

✉ Namhyun Kang  
nhkang@pusan.ac.kr

Guo Xian  
guoxian1989@gmail.com

- <sup>1</sup> Department of Materials Science and Engineering, Pusan National University, Busan 46241, Republic of Korea
- <sup>2</sup> Titanium Department, Korea Institute of Material Science, Gyeongsangnam-do, Changwon 51508, Republic of Korea
- <sup>3</sup> Yonsei University KIURI Institute, Yonsei University, Seoul 03722, Republic of Korea
- <sup>4</sup> Super-TIG Welding Co. Ltd, Busan 46722, Republic of Korea

Currently, several studies have been conducted on the columnar-to-equiaxed transition adopted in the AM process. Amongst them, pre-processing, in-processing and post-processing are the most common methods developed [10–15]. Pre-processing refers to the addition of alloying elements, such as copper and silicon [12, 14], which induce the transformation and refinement of grains through controlled solidification. Post-processing involves an additional treatment, such as rolling [13] or ultrasonic impact [15], to apply the stress and strain required to induce a greater driving force for post-welding recrystallisation. However, for Ti64, there are no effective solutions to manipulate the welding parameters for generating equiaxed grain structures during processing. Although low heat input was introduced to produce equiaxed prior- $\beta$  grains by reducing the current in the arc welding, the mechanism of solidification morphology remains unclear in the WAAM process, which has a large deposition along the building direction [11].

This study aims to determine how the heat input affects the morphology of prior- $\beta$  grains and mechanical properties of WAAM components. Fundamental solidification theories using the calculated thermal history were implemented to explain the transition of solidification morphology with respect to heat input. Moreover, the relationship between the microstructure and mechanical properties was analysed in detail.

## 2 Experimental and simulation methods

### 2.1 Materials and WAAM process

WAAM specimens were manufactured with a GTAW using a 1.6-mm diameter Ti64 consumable. Table 1 lists the processing parameters used in this study, where two heat input

**Table 1** Welding conditions of specimens H and L

Welding condition	H	L
Current (A)	250	180
Voltage (V)	21	13.8
Welding speed (m/s)	$5 \times 10^{-3}$	
Type of current	Continuous wave current	
Electrode type	Tungsten electrode 2% + Thoriated (2% Th)	
Electrode diameter (mm)	4	
Feed rate (m/s)	$3.15 \times 10^{-2}$	
Heat input (J/m)	$10^6$	$5 \times 10^5$

*H* higher heat input, *L* lower heat input

conditions (H and L) are considered. The chemical composition of the filler metal is shown in Table 2. To maintain the Ti64-welding rod feed rate and welding speed ( $5 \times 10^{-3}$  m/s), high and low arc currents of 250 A and 180 A were applied, respectively, corresponding to heat inputs of  $10^6$  J/m (H) and  $5 \times 10^5$  J/m (L). The resulting specimens were built as a single-bead wall with a width of ~10 mm for each layer. Argon gas (Ar, 99.99%) was used for arc torch and trailing shield for welding Ti64 to prevent oxidation. The experimental setup and GTAW with trailing shield (marked by red circle) are shown in Fig. 1a and b, respectively. After the arc extinguished, the shield for arc torch was terminated and that for trailing was operated until the specimen was cooled down to ~800 °C. The collapse of the WAAM structure and enlargement of grains were avoided by maintaining the interpass temperature below 100 °C. The interval time was increased as the layer thickness increased.

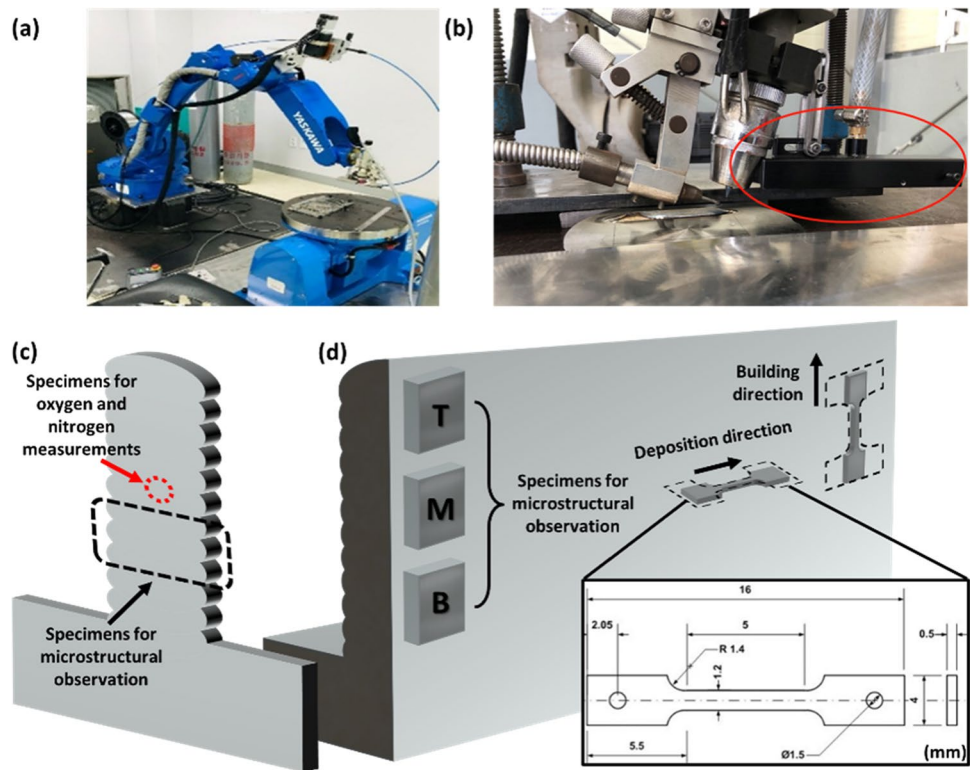
### 2.2 Characterisation

Figure 1c and d shows the preparation of the specimens for characterisation. The Ti64 deposits were cut into half along the build and deposition directions. The transverse cross-section for the deposition direction was observed to measure the weld pool and heat-affected zone (HAZ) shape. The prior- $\beta$  grains were more easily recognised in the longitudinal cross-section along the deposition direction. Specimens for microstructural observation, denoted as T, M and B, represent the top, middle and bottom parts along the building direction, respectively. All of the samples were polished using a 0.04- $\mu$ m colloidal silica suspension and were etched using Kroll's reagent to reveal the grain boundaries. The prior- $\beta$  grains, HAZ bands and  $\alpha$  phase were examined by light optical microscopy (LOM) and field-emission scanning electron microscopy (FE-SEM; Zeiss, Gemini 500). Electron backscatter diffraction (EBSD) was conducted to observe the  $\alpha$ -phase mapping by applying an accelerating voltage of 20 kV, probe current of 16 nA, step size of 4.5  $\mu$ m, working distance of 15 mm and sample tilt angle of 70°. The orientation information of the  $\beta$  phase was reconstructed from the  $\alpha$ -phase results obtained from the EBSD data. Transmission electron microscopy (TEM; TALOS F200X, 200 kV) was used for phase identification and orientation determination. To ensure the observation of the hardened phases (secondary  $\alpha$ ), a focused ion beam (FIB; Thermo Fisher) with a gallium (Ga) ion source was used to prepare the TEM samples (5  $\mu$ m  $\times$  5  $\mu$ m  $\times$  100 nm) directly from specimens H and L. The O and N contents were averaged from 6 measurements for each specimen. Finally, the

**Table 2** Chemical composition of the filler metal (wt. %)

	Al	V	Fe	Cr	Mg	Ni	Ti
Wire	5.839	3.837	0.09	0.004	0.002	0.001	Bal.

**Fig. 1** Experimental setup and GTAW with trailing shield (red circle) in (a) and (b) and preparation of the specimens for O and N contents, metallographic observation and tensile test in (c) transverse and (d) longitudinal cross-sections



oxygen (O) and nitrogen (N) content were measured by an ELTRA analyser using inert gas fusion in an impulse furnace at temperatures exceeding 3000 °C. The O and N contents were confirmed using the standard reference. Moreover, the as-built Ti64 deposits were cut into specimens in the deposition and building directions to evaluate their tensile properties. Figure 1d demonstrates the location and dimensions of the tensile specimens. According to the ASTM E8/E8M-21 standard, the tensile specimens were rescaled using the proportion with a gauge length, width and thickness of 5 mm, 1.2 mm and 0.5 mm, respectively. Tensile testing was performed on at least four specimens for each welding condition with an initial strain rate of  $0.5 \times 10^{-4} \text{ s}^{-1}$  (Shimadzu).

### 2.3 Thermal simulation of WAAM deposits

To simulate the Ti64 deposition process, the finite-element method was used to construct a thermal model using SYSWELD (ESI). Figure 2a and b shows the duplicated morphology of 10 layers deposited for the thermal model of specimens H and L, respectively, which corresponds to the experimental morphology observed. The height and width of the deposition block models were measured on the WAAM deposits for each layer. Figure 2c and d shows the models of the reconstructed mesh and double-ellipsoidal heat source, respectively. The mesh became finer as it approached the weld pool, thus, reducing the calculation

time for the model. Table 3 lists the parameters used to construct the model. The mesh geometry was established close to a hexahedron, and the size of the mesh was approximately  $1 \text{ mm}^3$ .

All the elements of the deposited layers were deactivated at the beginning of the analysis. Then, the elements were activated by layers to simulate metal deposition. The governing differential equation for transient thermal analysis can be expressed as [16]:

$$\rho c_p \frac{\partial T}{\partial t} = \frac{\partial}{\partial x} \left( k_x \frac{\partial T}{\partial x} \right) + \frac{\partial}{\partial y} \left( k_y \frac{\partial T}{\partial y} \right) + \frac{\partial}{\partial z} \left( k_z \frac{\partial T}{\partial z} \right) + \dot{q} \quad (1)$$

where  $\rho$  is the density of the conducting medium;  $c_p$  is the specific heat of the medium;  $k_x$ ,  $k_y$  and  $k_z$  are the thermal conductivities of the medium in the  $x$ -,  $y$ - and  $z$ -directions, respectively;  $t$  denotes time; and  $\dot{q}$  denotes the total heat input based on the Goldak’s model. Boundary and initial conditions are required to solve this differential equation. To simplify the finite-element thermal analysis, the following assumptions were made:

- 1) The initial temperature of the model is set at 20 °C.
- 2) The fluid flow in the molten pool is neglected.
- 3) The heat transfer from the model to the environment was defined at the surface of the model as convective heat dissipation and radiation to the environment (at 20 °C).

**Fig. 2** Modelling for (a) H construction and (b) L construction. (c) The finite-element mesh and (d) the double-ellipsoidal (Goldak’s) heat source model

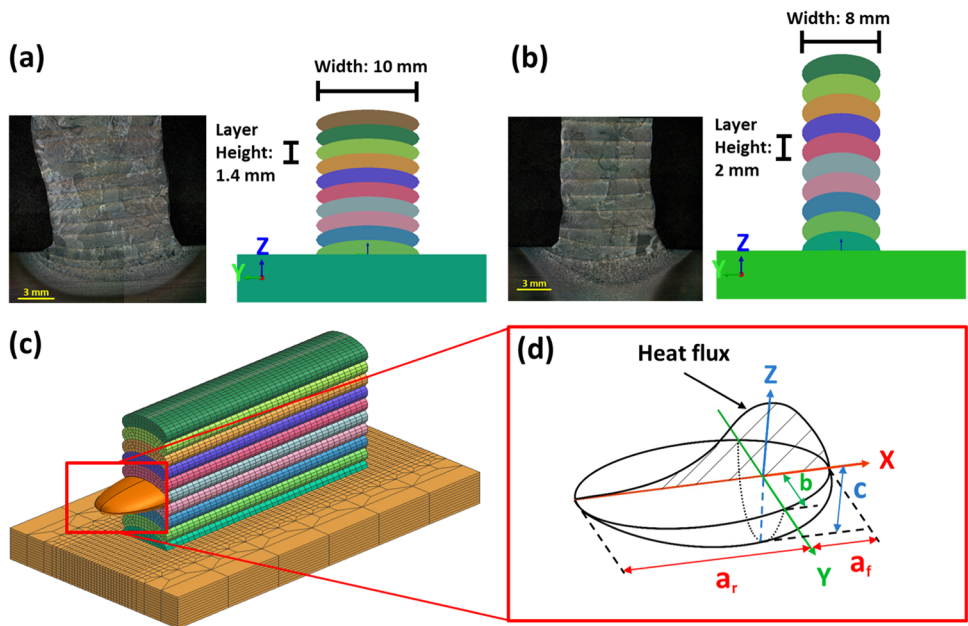


**Table 3** Modelling parameters applied in SYSWELD

Model parameters	Conditions
Material (base and weld metals)	Ti6Al4V
Density (kg/m <sup>3</sup> )	4.5
Specific heat (J/kg·K)	7.2
Thermal conductivity (W/m·K)	560
Layers	10
Thickness of base metal (mm)	10
Interpass temperature (°C)	100
Ambient temperature (°C)	31
Element size (mm <sup>3</sup> )	~ 1
Heat source parameter (af + ar)	12 mm
Heat source parameter (b)	4 mm
Heat source parameter (c)	2 mm
Arc type	TIG
Arc efficiency	60%

The power densities of the double-ellipsoid heat source during the WAAM process,  $q_f(x, y, z)$  and  $q_r(x, y, z)$ , which describe the heat flux distributions in the front and rear quadrants, respectively, are defined by Eqs. (2) and (3) [17]:

$$q_f(x, y, z) = \frac{6\sqrt{3}f_f Q}{a_r b c \pi \sqrt{\pi}} \cdot e^{-\frac{3x^2}{a_f^2}} \cdot e^{-\frac{3y^2}{b^2}} \cdot e^{-\frac{3z^2}{c^2}} \tag{2}$$

$$q_r(x, y, z) = \frac{6\sqrt{3}f_r Q}{a_r b c \pi \sqrt{\pi}} \cdot e^{-\frac{3x^2}{a_f^2}} \cdot e^{-\frac{3y^2}{b^2}} \cdot e^{-\frac{3z^2}{c^2}} \tag{3}$$

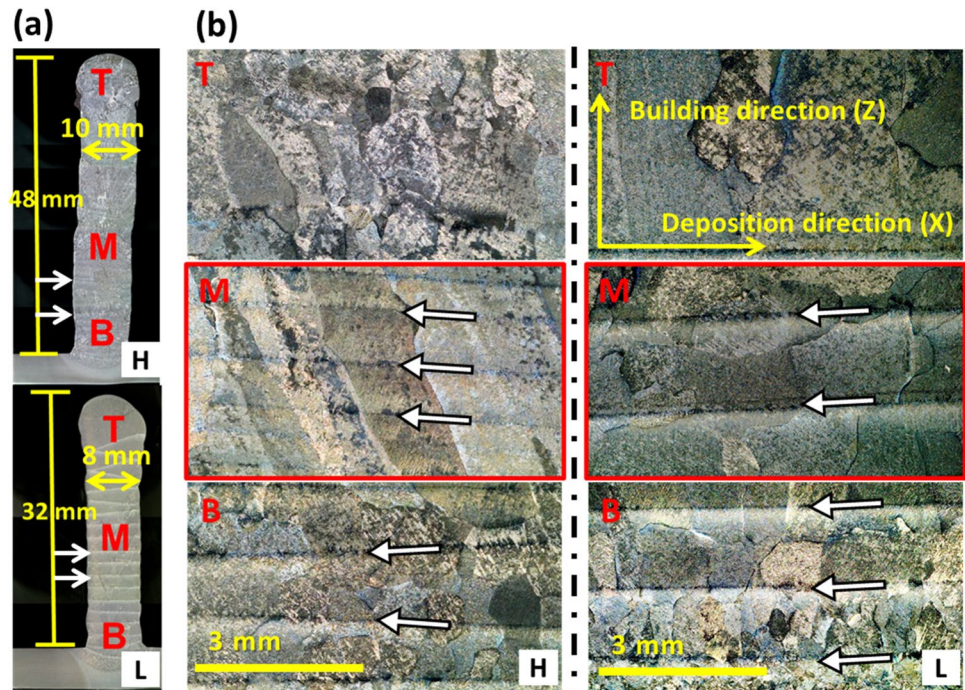
In this model,  $Q$  represents the effective heat power [W] and is expressed as  $Q = \eta \cdot U \cdot I$ . Here,  $\eta$ ,  $U$  and  $I$  represent the efficiency, welding voltage [V] and current [A], respectively. The variables  $f_f$  and  $f_r$  are the proportional coefficients at the front and rear ellipsoids of the heat source, respectively ( $f_f + f_r = 2$ ). Meanwhile,  $a_f$ ,  $a_r$ ,  $b$  and  $c$  represent the length/width/depth of the front/rear double ellipsoidal heat source parameters that define the size and shape of the ellipses, respectively (Fig. 2d). Lastly,  $x$ ,  $y$  and  $z$  denote the local coordinates of the reconstructed models.

### 3 Results

#### 3.1 Solidification morphology for various heat inputs

Figure 3 presents typical macro and solidification morphologies in the transverse and longitudinal cross-sections of the WAAM deposits. All the deposits exhibited appropriate weldability without macro-defects, such as internal pores and cracks. The total height of the deposits and location to measure the microstructural morphology are shown in Fig. 3a. White HAZ bands denoted as white arrows (Fig. 3) and caused by  $\beta$ -transus temperature were observed for all conditions [18]. The total height of the specimen was approximately 48 mm in H and 32 mm in L. The height of each layer was approximately equal to the distance between two HAZ bands. The height of each layer for specimen H was ~1.4 mm, which was smaller than that for specimen L (~2 mm). The bead width in H (~10 mm) was wider than L (~8 mm). The solidification grains always show strong

**Fig. 3** Macro and solidification morphology observed for (a) transverse cross-sections and (b) longitudinal cross-sections of specimens H and L. White arrows denote HAZ bands



alignment with their preferred growth direction, which is perpendicular to the curved solid–liquid surface. Therefore, the longitudinal cross-sections (Fig. 3b) indicate that the prior- $\beta$  grains solidified from the fusion line. Equiaxed grains were observed in region B close to the base metal, regardless of the heat input. However, the various-grain morphology existed as it approached region M. The large heat input (H) produced larger columnar  $\beta$  grains than the other conditions. The grain aspect ratio in specimen L decreased dramatically in  $z$  (building direction) and  $x$  (deposition direction), reflecting the improved homogeneity of the prior- $\beta$  grain structure. Furthermore, region T of all the specimens comprised equiaxed grains.

To further identify the prior- $\beta$  grain boundary and assess any potential changes in the crystallographic texture, EBSD analysis was conducted on region M of the Ti64 deposits. The  $\beta$  phase is a high-temperature phase. When cooled to room temperature, the prior- $\beta$  grain boundary transformed to  $\alpha$  grain, making it difficult to distinguish the prior- $\beta$  grain boundary from the EBSD alpha mapping. Several methods have been proposed in the literature to perform this procedure using the orientations measured from  $\alpha$  variants in EBSD scans [19–21]. Using the Burgers orientation relationship, the parent  $\beta$  grain orientation was reconstructed based on the knowledge of  $\alpha$ -phase orientations measured at room temperature using MTEX codes and the MATLAB software [21]. Figure 4a and c shows the inverse-pole figures for the  $\alpha$  phase measured by EBSD. Figure 4b and d shows the

inverse-pole figures for the  $\beta$  phase reconstructed from the  $\alpha$ -phase maps (Fig. 4a and c). Specimens H and L exhibited long columnar grains and large equiaxed grains, respectively. The EBSD-reconstructed  $\beta$  grains were consistent with the grain morphology measured by LOM (Fig. 3b). The grain sizes (i.e. the width of the columnar and equiaxed grains) in the deposition direction ( $x$ ) of the reconstructed  $\beta$  phase are 1.5 mm and 2 mm for specimens H and L, respectively.

### 3.2 Microstructure for various heat inputs

Figure 5 shows the representative microstructure observed in region M for each specimen. Specimen H fully comprises  $\alpha'$  martensite, which is characterised by long orthogonally oriented martensitic plates. The rectangular grid structure, indicated by the black dotted lines (enlarged figure in Fig. 5a), is a typical feature of  $\alpha'$  martensite [22]. Particularly, some white and lathy lines were observed in the  $\alpha'$  martensite. The phase between the lines nucleated or grew into the primary  $\alpha$  or  $\alpha'$  martensite, known as secondary  $\alpha$  [23], which is formed upon cooling during the sub-transus thermal cycle; it has morphological forms similar to those of primary  $\alpha$ . More  $\alpha'$  martensite with additional secondary  $\alpha$  resulted in large hardness of 348 Hv for specimen H. However, distinct from  $\alpha'$  martensite, primary  $\alpha$ , including colony and basketweave, is formed during cooling from a peak temperature above the  $\beta$  transus with a relatively lower

**Fig. 4** Prior- $\beta$  grains of specimens (a, b) H and (b, d) L. (a) and (c) are measured by EBSD, whilst (b) and (d) are reconstructed from the  $\alpha$ -phase mapping of EBSD

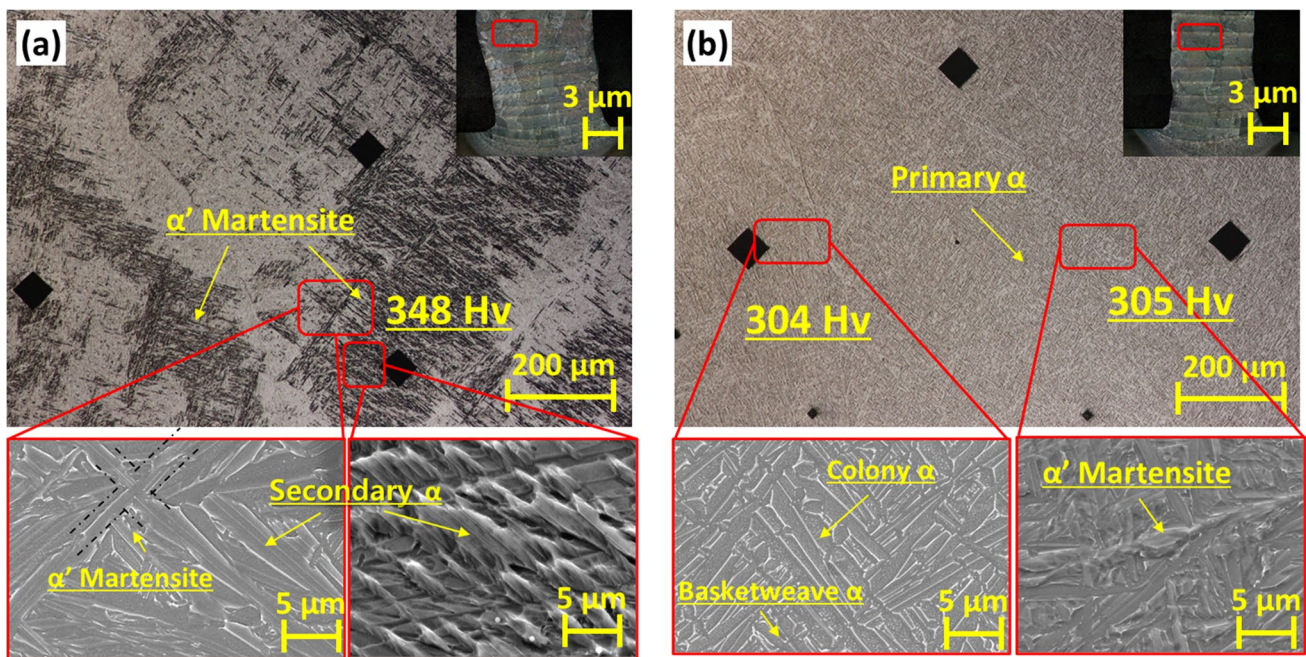
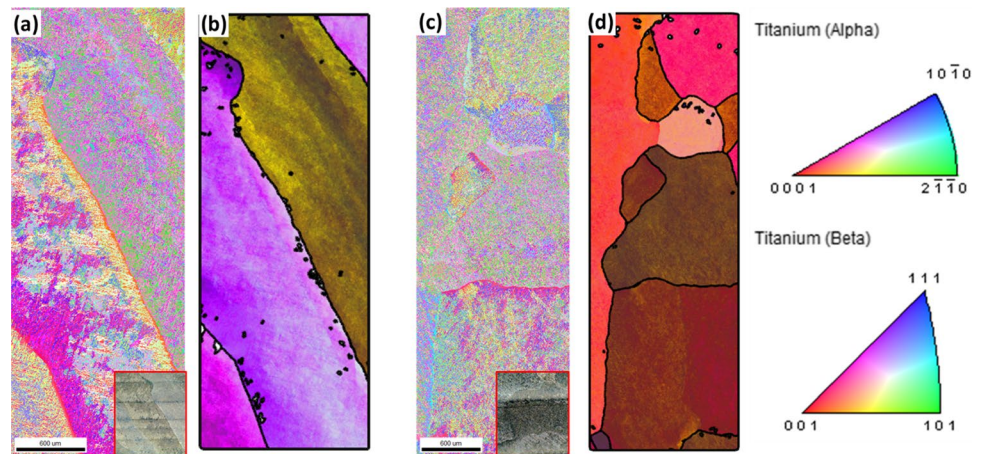


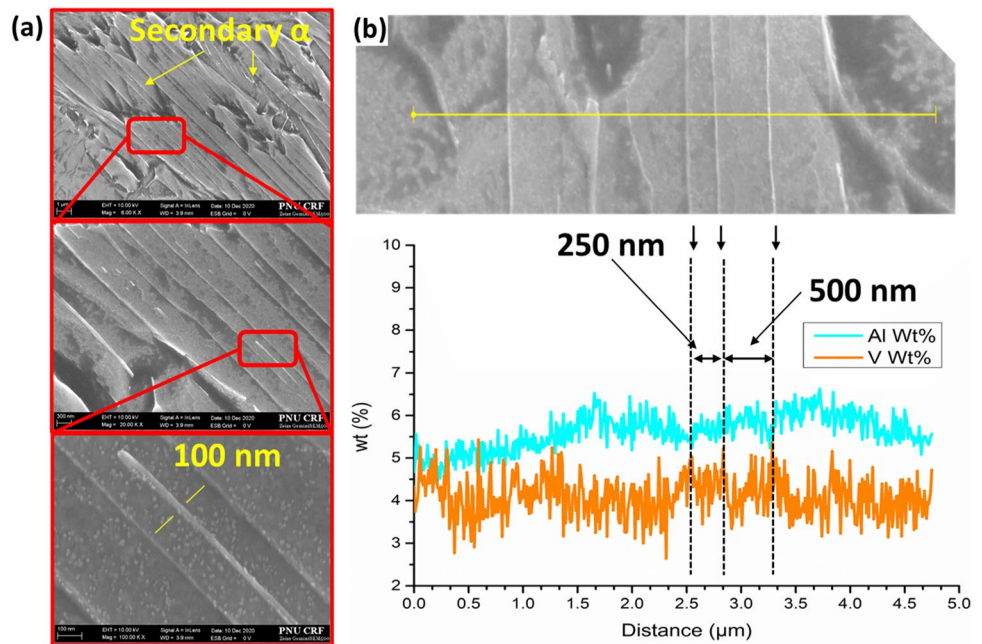
**Fig. 5** Microstructural variation of specimens (a) H and (b) L

cooling rate. Despite a higher cooling rate in the solidification range (1600–1660 °C), specimen L produced a large volume fraction of primary  $\alpha$  and a few  $\alpha'$  martensite, as shown in Fig. 5b, which exhibited a lower hardness of approximately 304 Hv relative to specimen H. The relation of microstructure, mechanical property and cooling rate in solidification and  $\beta$ -transus ranges will be explained later in the discussion part.

To clearly identify the secondary  $\alpha$  in the  $\alpha'$  martensite, high-resolution SEM images and EDX

measurements were taken from a number of  $\alpha'$  martensite with white and lathy lines. Figure 6a and b presents the high magnification SEM images of specimen H and the vanadium (V) and aluminium (Al) concentration profiles across these secondary  $\alpha$  by EDX line analysis, respectively. The white lathy area, which was determined from the morphology and element variation, showed that the line was residual  $\beta$ , and ultra-fine  $\alpha$  was produced in the residual  $\beta$ . The residual  $\beta$  contains high V content and low Al content because V is a  $\beta$  stabiliser and Al is

**Fig. 6** SEM–EDX line scan across secondary  $\alpha$  from specific position with higher hardness in specimen H. **(a)** High magnification SEM and **(b)** V and Al concentrations across the secondary  $\alpha$



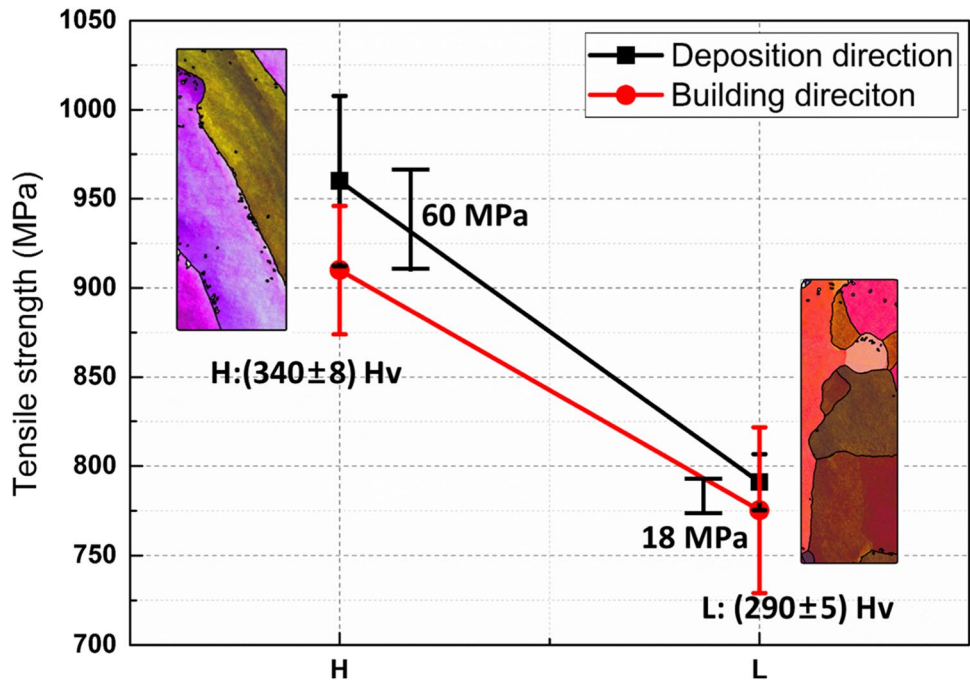
an  $\alpha\text{n}$  stabiliser. The average thickness of these  $\alpha$  was approximately 300 nm, and the minimum thickness of the residual  $\beta$  reached 100 nm.

### 3.3 Anisotropic tensile strength for various heat inputs

Figure 7 presents the tensile properties of the WAAM deposits. The black squares and red dots represent the tensile

strength of the deposition and building directions, respectively. Specimen H produced a building direction with a tensile strength smaller than that of the deposition direction. The difference of  $\sim 160$  MPa in tensile strength matched the gap in hardness ( $\sim 50$  HV). The anisotropic variation of the tensile strength of specimen H with columnar grains was larger by approximately 42 MPa than that of specimen L with large equiaxed grains. Specimen L showed the almost identical strength, regardless of the direction, owing to equiaxed

**Fig. 7** Anisotropic tensile strength along the building and deposition directions of specimens H and L



grains. The reason specimen H has larger hardness and tensile strength values than specimen L will be discussed later.

### 3.4 Thermal simulation for various heat inputs

The thermal distributions of specimens H and L were successfully simulated, as shown in Fig. 8. Various colours correspond to various temperatures. The grey area below the arc indicates a temperature above 1660 °C, whilst the pink area indicates the mushy zone, with temperatures at approximately 1600–1660 °C. Figure 8a and b demonstrates the weld pool shape in a stringer trajectory with various heat inputs (H and L, respectively). The trajectory followed a straight path, and the weld pool remained elliptical. The length and width of the weld pool for specimen H (Fig. 8a) were slightly larger than those of specimen L (Fig. 8b).

The thermal distribution of the WAAM deposit was validated through experiments (Fig. 8c and d). It was difficult to identify the fusion boundary in the microstructures of the WAAM cross-sections (Fig. 3) because the WAAM deposits solidified epitaxially from the fusion line with no variation in the microstructural morphology. Furthermore, the previously deposited layer remelted and was covered by the newly deposited

layer. This phenomenon makes it more challenging to recognise and confirm fusion boundary in the WAAM deposits. The white bands observed in Fig. 3 were acknowledged as a HAZ band, representing the  $\beta$ -transus temperature of approximately 1006 °C in Ti64 [18]. Therefore, the HAZ band, specifically the last one at the top of the specimen, is the optimal position for evaluating the simulation result because the distance from the top is stable, even with remelting and metal flow. In Fig. 8d, the last HAZ band was located approximately 7.2 mm from the top surface. In the simulation of the thermal distribution, the border line between yellow and green represents 1006 °C. The distance from the top to the border line of 1006 °C was approximately 7 mm, which is consistent with the experimental results.

## 4 Discussion

The grain morphology and microstructure during solidification were identified in the Ti64 WAAM specimens. In the WAAM process, we highlight the thermal simulation to illustrate the mechanism of the equiaxed grains and discuss the reason for the larger tensile strength of specimen H with large columnar grains.

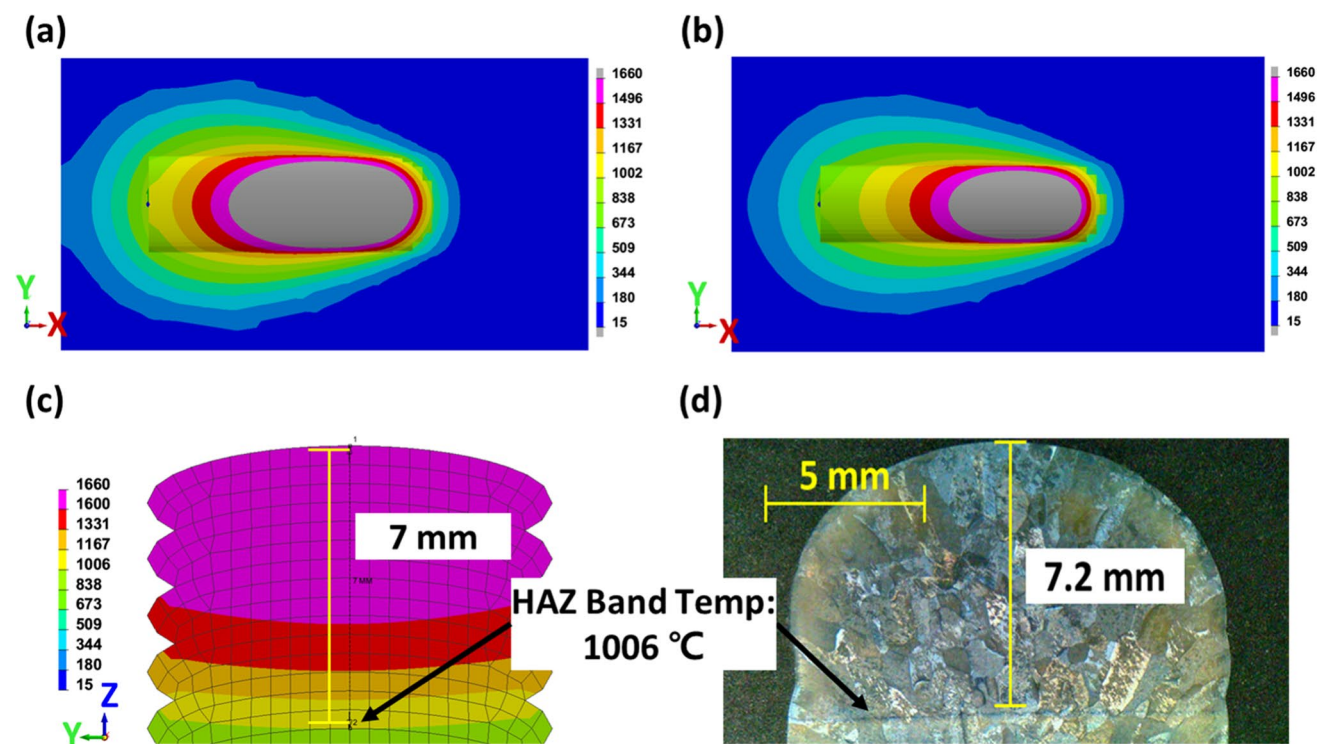


**Fig. 8** Weld pool shape simulated for various conditions and its validation for (a) H and (b) L. HAZ-bands height in the (c) simulation and (d) experiment



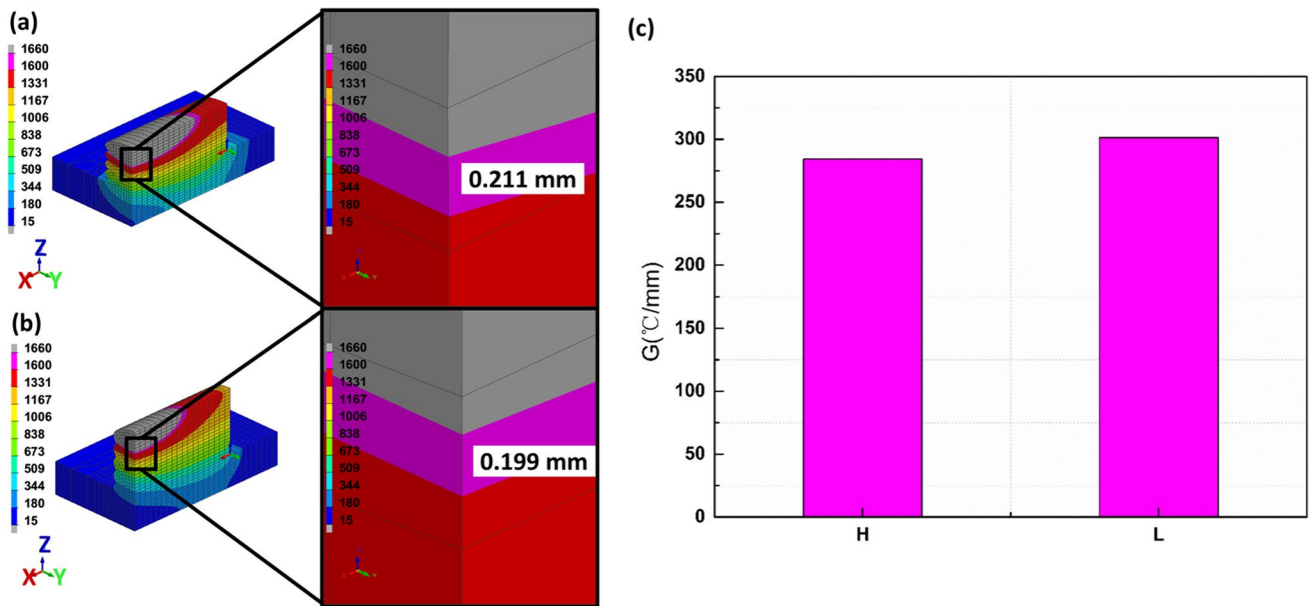


**Fig. 9** Temperature distribution and distance from liquidus to solidus for various heat inputs: (a) H and (b) L. (c) Temperature gradient ( $G$ ) along the building direction

### 4.1 Effect of heat input on grain morphology

#### 4.1.1 Temperature gradient ( $G$ ) simulated for various heat inputs

The temperature gradient ( $G$ ) played a significant role in solidification. Figure 9 a and b demonstrates the morphologies of region M (fifth layer) in specimens H and L, respectively. The pink area of the solidification range (1600–1660 °C) was extracted to calculate  $G$ . The distances between the liquidus and solidus in specimens H and L were 0.211 and 0.199 mm, respectively. The value of  $G$  was calculated using Eq. (4):

$$G = \frac{T(\text{liquidus}) - T(\text{solidus})}{\text{Distance}(\text{liquidus} - \text{solidus})} \quad (4)$$

Figure 9c compares the  $G$  values of specimens H and L, and the values for both the specimens are approximately 300 °C/mm. Therefore, the deviation of  $G$  has minor impact on the solidification process for various heat inputs in this study. The simulation results are consistent with those of a previous study, which reported that it was difficult to change the temperature gradient by altering the welding conditions in WAAM [24]. The value of  $G$  is usually stable for one type of heat source, even though the welding condition varies.

#### 4.1.2 Cooling rates simulated for various heat inputs

The cooling rate in the solidification range is also a significant factor in predicting the grain morphology during solidification. Figure 10 shows the thermal profile calculated from the fifth deposited layer of specimens H and L. The centre of the bottom-fusion zone represents the node location used to extract the temperature profile. The red and blue circles indicate the node location for specimens H and L, respectively. The solidification range was 1600–1660 °C, as indicated by the pink-coloured box. Consecutive thermal cycles for six depositions are plotted starting from the fifth to the tenth layer. By enlarging the area of the last cycle over 1660 °C (seventh cycle for specimen H and sixth cycle for specimen L), we approximated the cooling rate of specimen L to be 429 °C/s, which is approximately two times faster than that of specimen H (~201 °C/s). Therefore, the equiaxed grains are easily produced in specimen L (lower heat input) owing to its faster cooling rate than that of specimen H.

#### 4.1.3 Solidification rates for various heat inputs

Along with the temperature gradient ( $G$ ), the solidification rate ( $R$ ) can predict the solidification morphology from the Ti64 solidification map [25]. The value of  $G$  was extracted from the WAAM simulation (Fig. 8c), and  $R$  was calculated using Eq. (5):

**Fig. 10** Simulation of cooling rates in specimens H and L

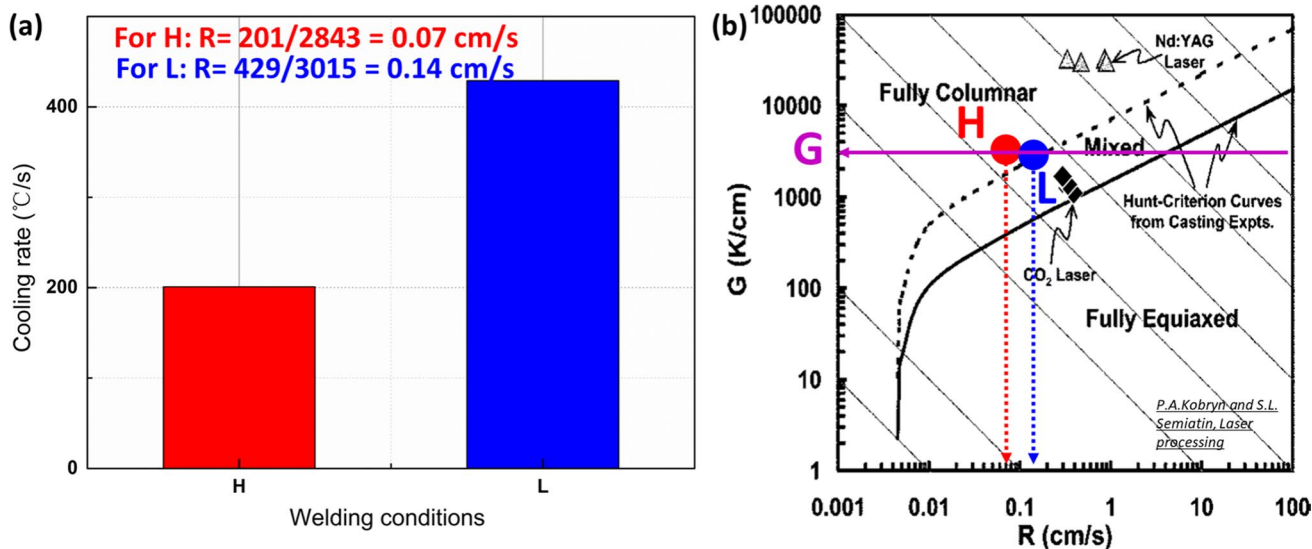
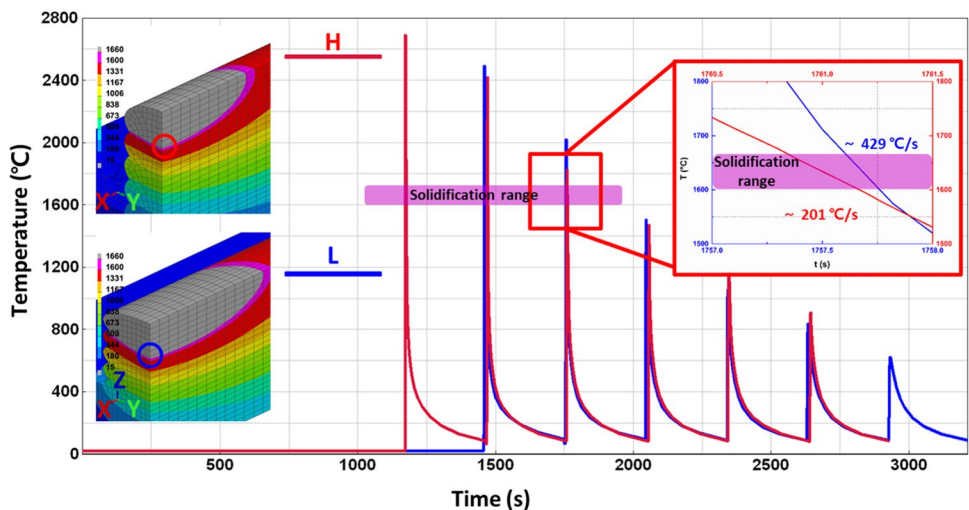


**Fig. 11** Simulation of the cooling and solidification rates ( $R$ ) in the Ti64 solidification map: (a) the cooling rate and the corresponding  $R$  value. (b) The solidification parameters of  $G$  and  $R$  compared for specimens H and L in Ti64 solidification map [25]

$$R = \frac{\text{Cooling rate}}{G} \tag{5}$$

Figure 11a presents the  $R$  values of specimens H and L, which are 0.07 and 0.14 cm/s, respectively, indicating that the  $R$  value of specimen L is two times larger than that of specimen H. Figure 11b shows the  $R$  (Fig. 11a) and  $G$  (Fig. 8c) values that were incorporated into the Ti64 solidification map [25]. The pink line represents constant  $G$  (~3000 K/cm); the red and blue dotted lines represent the  $R$  values for specimens H and L, respectively. Specimen H is in the region of fully columnar morphology, which was associated with the columnar grains (Figs. 3b and 4a), and specimen L is in the range of mixed morphology of columnar and

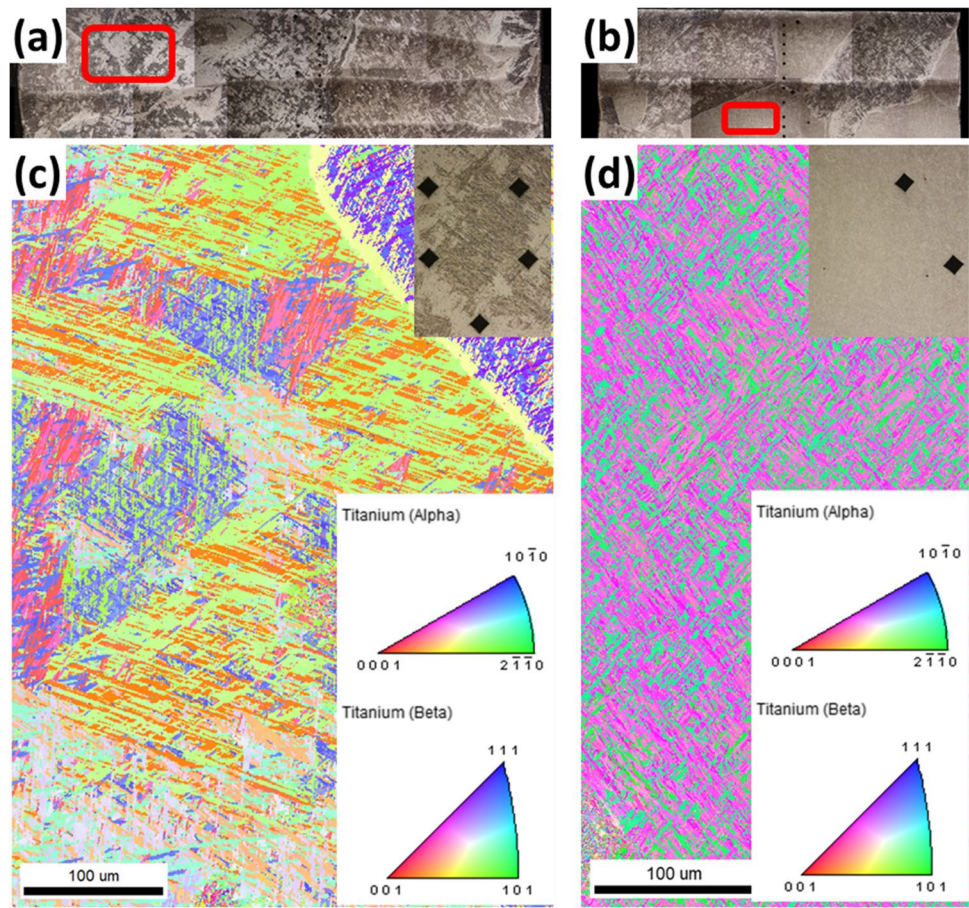
equiaxed grains. Therefore, the low heat input (L) produced more equiaxed grains than the high heat input (H).

## 4.2 Effect of heat input on microstructure

### 4.2.1 Precise characterisation of fine secondary $\alpha$

In  $\alpha + \beta$  titanium alloys, such as Ti64, secondary phase transformations always occur during heat treatments where heating and cooling occur below the  $\beta$  transus. During heating, the primary  $\alpha$  dissolves in  $\beta$ , forming a mixture of primary  $\alpha$  and  $\beta$ . During cooling, the newly formed regions of  $\beta$  decompose into secondary  $\alpha$ , producing a mixture of residual  $\beta$ , primary  $\alpha$  and

**Fig. 12** Grain morphology and  $\alpha$  orientation maps for specimens (a, c) H and (b, d) L measured using LOM and EBSD. EBSD results show the enlarged microstructure from the red boxes of LOM

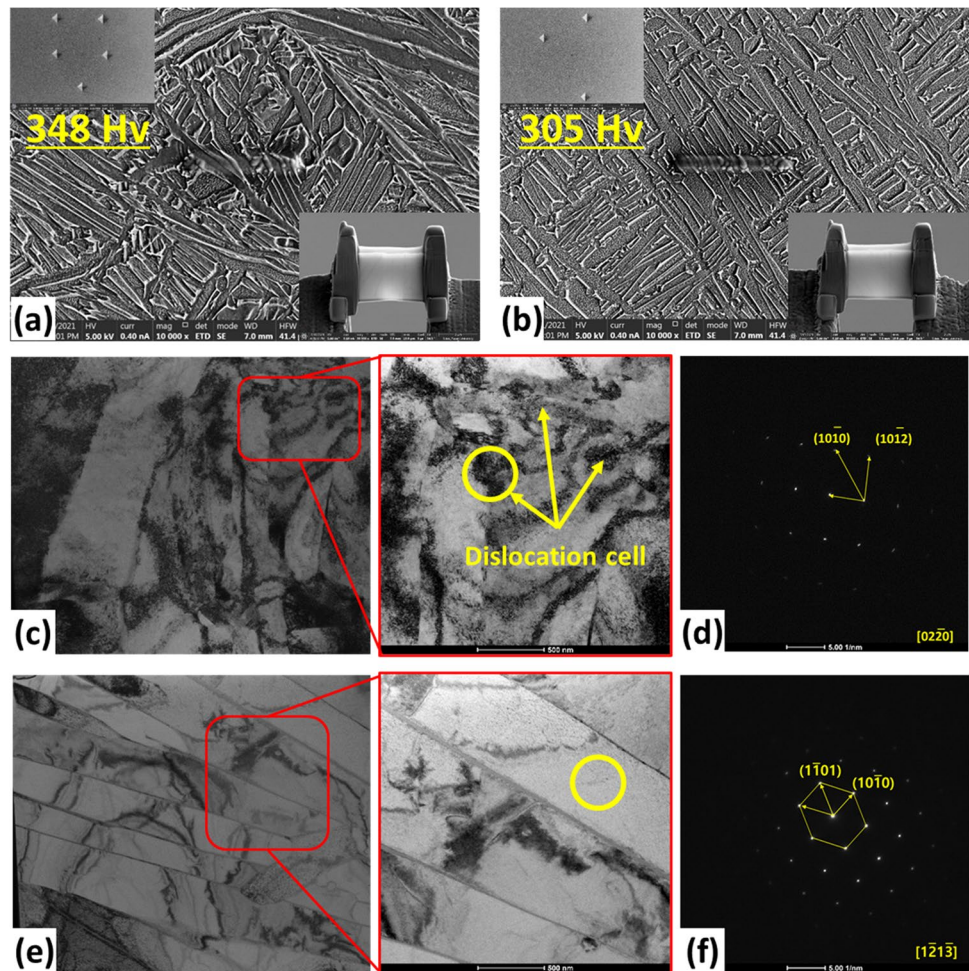


secondary  $\alpha$ . In Ti64 alloys, the  $\beta$  phase transforms into several  $\alpha$ -phase morphologies based on the cooling rate. Typical cooling rates for the transformation products have recently been studied, and the microstructure in WAAM falls into the mixture phase region (that is,  $\alpha' + \alpha_{\text{massive}} + \alpha$ ) [22]. The  $\alpha_{\text{massive}}$  phase is primarily observed in the region reheated above  $\beta$ -transus temperature of EBW [26].

Figure 12 shows the microstructure of specimens H and L observed through LOM and EBSD to analyse the  $\alpha$ -phase morphologies in detail. The  $\alpha$ -orientation was inhomogeneous in all the prior- $\beta$  grains of specimen H (Fig. 12a) compared to that of specimen L (Fig. 12b) by LOM. Moreover, we can clearly identify the size of the secondary colony  $\alpha$  using  $\alpha$ -orientation maps of EBSD. Specimen H had at least four types of secondary  $\alpha$  colonies with various orientation relationships. In summary, new secondary- $\alpha$  colonies were observed more in specimen H than in specimen L. More secondary  $\alpha$  nucleated in the primary specimen causing an improvement in the mechanical properties of specimen H. More  $\alpha$  colonies partitioned  $\beta$  grains into small colonies and complex relationships, increasing the hardness and tensile strength of the specimen.

Previous studies have shown that the microstructure induces a variation in hardness and tensile strength [27]. A large volume fraction of  $\alpha'$  martensite, containing secondary  $\alpha$  and/or small colonies with secondary  $\alpha$ , can improve the overall mechanical properties. To further analyse the microstructure, two TEM samples were prepared using FIB from the maximum hardness regions in both specimens H (348 Hv) and L (305 Hv), as shown in Fig. 13a and b. The hardness marks in Fig. 13a and b are consistent with the inset of Fig. 12c and d. The TEM images of the FIB sample are shown in Fig. 13c and e for specimens H and L, respectively. Specimen L shows more  $\alpha$  plates (Fig. 13e), and specimen H have irregular  $\alpha$  plates with dark regions. The plates and the dark region were identified as the hcp phase, according to the selected area electron diffraction (SAED) patterns shown in Fig. 13d and f with zone axis  $[0\ 2\ -2\ 0]$  and  $[1\ -2\ 1\ -3]$ , respectively. The dark region around the secondary  $\alpha$  indicated high-density and tangled dislocation cells [28], which could effectively improve the hardness and tensile strength. However, only a few dislocation cells were observed in specimen L, as indicated by the yellow circle. The grain boundary of the  $\alpha$  plate was clear and almost parallel to a colony with a minor dislocation line. A large number of dislocations

**Fig. 13** FIB specimens prepared for (a) H and (b) L. The TEM bright-field images with SAED patterns for (c, d) H and (e, f) L



in specimen H resulted in large hardness and tensile strength values. The reason specimen H with a high heat input and slow cooling rate would have a large number of dislocations will be discussed in Sect. 4.2.2.

#### 4.2.2 Mechanism of microstructural evolution of secondary $\alpha$

Unlike the traditional heat input effect in welding, there is less effect in WAAM solidification. A higher heat input with a higher current produced a wider weld pool, broadening the deposition width of each layer [29]. Therefore, at a constant welding speed and feeding rate, the deposition height in specimen H was smaller than that in specimen L because of the constant deposition area, as shown in Fig. 2a and b. The variation in the weld pool and deposition shapes is owing to the remelting and cooling times. The effects of the deposition shape on the microstructure and mechanical properties are as follows:

**Variation of oxygen and nitrogen content with respect to heat input** Oxygen and nitrogen are key impurities or alloying elements that affect the microstructure and mechanical

properties of Ti64. Previous studies have expressed O equivalence as [30]:

$$[O]_{eq} = [O] + 2[N] + 2/3[C](wt\%) \quad (6)$$

Oxygen and nitrogen are an alpha stabiliser and the increment of O and N contents raises the  $\beta$ -transus temperature

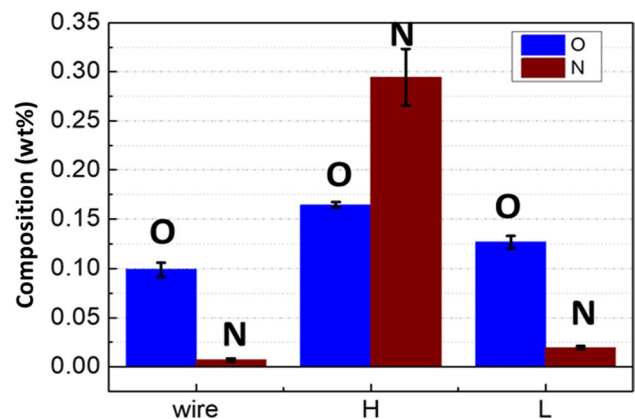
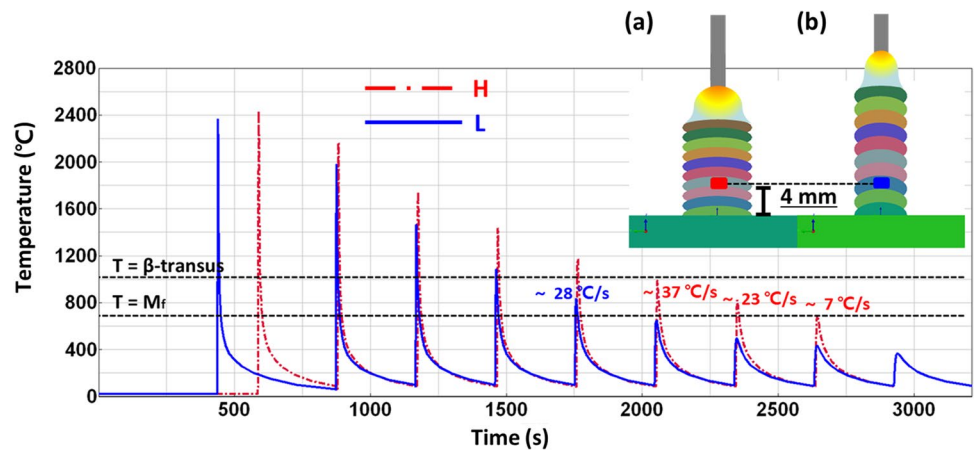


**Fig. 14** O and N contents of the filler wire, specimen H (high heat input) and specimen L (low heat input)

**Fig. 15** Simulation of cooling rates and 10 thermal cycles during secondary  $\alpha$  transformation in specimens (a) H and (b) L



[30]. Therefore, the martensitic transformation temperature increases with increasing the O and N contents and the martensitic phases can be induced or promoted by high concentrations of O and N in Ti64 alloys.

Figure 14 shows the O and N concentrations measured for the filler wire, specimen H and specimen L. Before welding, the O and N concentrations in the filler wire were lower (O: 0.1 wt% and N: 0.001 wt%) than those in specimen H (O: 0.16 wt% and N: 0.3 wt%) and specimen L (O: 0.13 wt% and N: 0.003 wt%) after welding. This is because during melting and solidification, some O and N in the air dissolve into the deposited metal. Compared with specimen L, specimen H showed a large amount of O and N, possibly owing to the larger and wider weld pool. The N content increased significantly more than the O content, and this was attributed to the composition of air, wherein the N concentration is approximately three times larger than the O concentration. The high concentrations of O and N in specimen H promoted the martensitic-phase transformation with a large number of dislocations and improved the hardness and tensile strength [31].

**Effect of thermal cycles on the microstructural evolution of secondary  $\alpha$**  Temperature profiles were extracted from the same height of the deposits to clarify the correlation between the thermal history and evolution of secondary  $\alpha$ . Figure 15 shows the position used to calculate the thermal cycles, which is approximately 4 mm from the base metal for specimens H and L. Secondary  $\alpha$  phases are transformed below the  $\beta$  temperature (1006 °C) to 700 °C according to the Ti64 phase diagram. Specimen H (red dashed line) was exposed in the temperature range with more thermal cycles than specimen L (blue line). According to the calculation, the cooling rate of specimen H was  $\sim 37$  °C/s, which was higher than that of specimen L ( $\sim 28$  °C/s) within the secondary  $\alpha$  transformation temperatures. However, according to the previous studies and phase diagram [23], the cooling rate of 20 °C/s is a key transformation boundary to vary the solidification morphology of alpha phase. Therefore, more thermal cycles and rapid cooling rates result in more  $\alpha$  colonies and fine secondary  $\alpha$  for specimen H [23, 32].

**Fig. 16** Schematics of the primary and secondary  $\alpha$  evolution during the thermal cycles

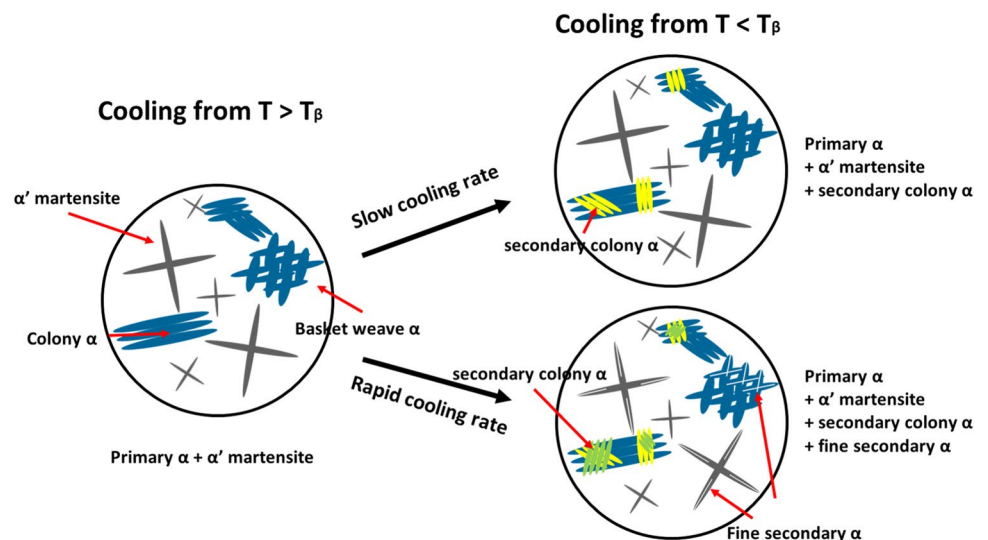


Figure 16 illustrates the microstructural evolution mechanisms for various heat inputs. During the cooling process at temperatures above the  $\beta$  transus, primary  $\alpha$  and  $\alpha'$  martensite appeared. Below the  $\beta$  transus temperature, some  $\alpha'$  martensite decomposed into metastable  $\beta$  with retained dislocations during rapid reheating, which was also revealed by TEM. Consequently, the microstructure that contains retained  $\beta$  transformed into a new secondary  $\alpha$ . Therefore, the yellow one represents the secondary alpha and the green one means another secondary alpha produced in the next thermal cycle. It was associated to the various  $\alpha$ -orientations in secondary  $\alpha$  colonies for specimen H (Fig. 12a). The morphology of the secondary  $\alpha$  (colony or fine) depends on the cooling rate. Rapid cooling rates (H) in the secondary  $\alpha$  transformation temperatures produced higher volume fraction of secondary  $\alpha$ . Hence, the resulting microstructure of specimen H consisted of primary  $\alpha$ ,  $\alpha'$  martensite, secondary  $\alpha$  colony and fine secondary  $\alpha$ .

## 5 Conclusion

The in-processing parameter heat input has been discussed in relation to the grain morphology and tensile strength of the Ti64 WAAM deposits. The primary findings are as follows:

1. For a constant feeding rate and welding speed, the weld pool shape in the high heat input specimen (H) became wider and shallower.
2. Compared with a high heat input (specimen H), a low heat input (specimen L) modified the grain morphology from columnar to equiaxed grains, thereby reducing the anisotropic tensile strength. The faster solidification rate ( $R$ ) in solidification range (1600–1660 °C) induced the transformation of the columnar grains to the equiaxed grains for specimen L.
3. Specimen H exhibited a higher hardness and tensile strength values for the following reasons. The large amounts of O and N in specimen H promoted the  $\alpha'$  martensitic phase transformation. During the secondary  $\alpha$  transformation temperature (700–1006 °C), a more rapid cooling rate and thermal cycles contributed to a higher volume fraction of fine and secondary colony  $\alpha$  with a tangled dislocation.

**Acknowledgements** This work was supported in part by the Ministry of Science, ICT and Future Planning of Korea through the National Research Foundation of Korea (NRF) Future Material Discovery Project of (NRF-2016M3D1A1023534) and by the Ministry of Trade, Industry and Energy (MOTIE, Korea) through the Technology Innovation Programme (20004932).

## Declarations

**Conflict of interest** The authors declare no competing interests.

## References

1. Rodrigues, T.A. Duarte, V. Miranda, R.M. Santos, T.G. Oliveira, J.P. Current status and perspectives on wire and arc additive manufacturing (WAAM), *Materials* (Basel) 12(7) (2019).
2. Knezović, N. Topić, A. Wire and arc additive manufacturing (WAAM) – a new advance in manufacturing, *New Technologies, Development and Application* 2019.
3. Herzog D, Seyda V, Wycisk E, Emmelmann C (2016) Additive manufacturing of metals. *Acta Mater* 117:371–392
4. Wu B (2018) A review of the wire arc additive manufacturing of metals: properties, defects and quality improvement. *J Manuf Process* 35:127–139
5. Choi S-W, Hong J, Park CH, Lee S, Kang N, Choi YS, Park JT, Ahn ST, Yeom J-T (2019) Manufacturing process of titanium alloys flux-metal cored wire for gas tungsten arc welding. *J Weld Join* 37(3):268–274
6. Huda, N. Kim, J.W. Ji, C. Nam, D.-G. Park, Y.-D. Determination of optimal weld parameter for joining titanium alloys by gas tungsten arc welding using Taguchi method, *Journal of Welding and Joining* (2021).
7. Park JH, Park SY, Cho SM (2019) A study on process development of deformation reduction in TIG overlay welding. *J Weld Join* 37(1):82–88
8. Wang F, Williams S, Rush M (2011) Morphology investigation on direct current pulsed gas tungsten arc welded additive layer manufactured Ti6Al4V alloy. *Int J Adv Manuf Technol* 57(5–8):597–603
9. Carroll BE, Palmer TA, Beese AM (2015) Anisotropic tensile behavior of Ti–6Al–4V components fabricated with directed energy deposition additive manufacturing. *Acta Mater* 87:309–320
10. Wang J, Lin X, Li J, Hu Y, Zhou Y, Wang C, Li Q, Huang W (2019) Effects of deposition strategies on macro/microstructure and mechanical properties of wire and arc additive manufactured Ti 6Al 4V. *Mater Sci Eng, A* 754:735–749
11. Wang, J. Lin, X. Li, J. Xue, A. Liu, F. Huang, W. Liang, E. A study on obtaining equiaxed prior- $\beta$  grains of wire and arc additive manufactured Ti–6Al–4V, *Materials Science and Engineering: A* 772 (2020).
12. Zhang D, Qiu D, Gibson M, Zheng Y, Fraser H, StJohn D, Easton M (2019) Additive manufacturing of ultrafine-grained high-strength titanium alloys. *Nature* 576:91–95
13. McAndrew AR, Alvarez Rosales M, Colegrove PA, Hönnige JR, Ho A, Fayolle R, Eyitayo K, Stan I, Sukrongpang P, Crochemore A, Pinter Z (2018) Interpass rolling of Ti-6Al-4V wire + arc additively manufactured features for microstructural refinement. *Addit Manuf* 21:340–349
14. John, D.H. St McDonald, S.D. Bermingham, M.J. Mereddy, S. Prasad, A. Dargusch, M. The challenges associated with the formation of equiaxed grains during additive manufacturing of titanium alloys, *Key Engineering Materials, Trans Tech Publ*, 2018, pp. 155–164.
15. Yang, Y. Jin, X. Liu, C. Xiao, M. Lu, J. Fan, H. Ma, S. Residual stress, mechanical properties, and grain morphology of Ti-6Al-4V alloy produced by ultrasonic impact treatment assisted wire and arc additive manufacturing, *Metals* 8(11) (2018).
16. Samad, Z. Nor, N.M. Fauzi, E.R.I. Thermo-mechanical simulation of temperature distribution and prediction of heat-affected zone

- size in MIG welding process on aluminium alloy EN AW 6082-T6, IOP Conference Series: Materials Science and Engineering 530 (2019).
17. Kik, T, Moravec, J, Svec, M. Experiments and numerical simulations of the annealing temperature influence on the residual stresses level in S700MC steel welded elements, *Materials* (Basel) 13(22) (2020).
  18. Ho A, Zhao H, Fellowes JW, Martina F, Davis AE, Prangnell PB (2019) On the origin of microstructural banding in Ti-6Al4V wire-arc based high deposition rate additive manufacturing. *Acta Mater* 166:306–323
  19. Humbert M, Gey N (2002) The calculation of a parent grain orientation from inherited variants for approximate (b.c.c.–h.c.p.) orientation relations. *J Appl Crystallogr - J APPL CRYST* 35:401–405
  20. Cayron C (2007) ARPGE: a computer program to automatically reconstruct the parent grains from electron backscatter diffraction data. *J Appl Crystallogr* 40(Pt 6):1183–1188
  21. Bachmann F, Hielscher R, Schaeben H (2010) Texture analysis with MTEX – free and open source software toolbox. *Solid State Phenom* 160:63–68
  22. Ahmed, T, Rack, H.J. Phase transformations during cooling in  $\alpha+\beta$  titanium alloys, *Materials Science and Engineering: A* 243 (1998).
  23. Kelly, S.M. Thermal and microstructure modeling of metal deposition processes with application to Ti-6Al-4V, 2004.
  24. Todaro CJ, Easton MA, Qiu D, Zhang D, Bermingham MJ, Lui EW, Brandt M, StJohn DH, Qian M (2020) Grain structure control during metal 3D printing by high-intensity ultrasound. *Nat Commun* 11(1):142
  25. Semiatin, P.A.K.a.S.L. The laser additive manufacture of Ti-6Al-4V, *Laser Processing* (2001).
  26. Lu SL, Qian M, Tang HP, Yan M, Wang J, StJohn DH (2016) Massive transformation in Ti–6Al–4V additively manufactured by selective electron beam melting. *Acta Mater* 104:303–311
  27. Yi H-J, Kim J-W, Kim Y-L, Shin S (2020) Effects of cooling rate on the microstructure and tensile properties of wire-arc additive manufactured Ti–6Al–4V Alloy. *Met Mater Int* 26(8):1235–1246
  28. Wu G, Feng C, Liu H, Liu Y, Yi D (2020) Fine secondary  $\alpha$  phase-induced strengthening in a Ti-5.5Al-2Zr-1Mo-2.5V alloy pipe with a Widmanstätten microstructure. *J Mater Eng Perform* 29(3):1869–1881
  29. M.a.f.N. SY Lee, Dr Ing, MAWS, MDVS, Analysis of TIG welding arc using boundary-fitted coordinates, Part B: *Journal of Engineering Manufacture* 209 (1995).
  30. Yan M, Xu W, Dargusch MS, Tang HP, Brandt M, Qian M (2014) Review of effect of oxygen on room temperature ductility of titanium and titanium alloys. *Powder Metall* 57(4):251–257
  31. Jaffee, H.R.O.a.R.I. The effects of carbon, oxygen, and nitrogen on the mechanical properties of titanium alloys, 1955.
  32. Yang J, Yu H, Yin J, Gao M, Wang Z, Zeng X (2016) Formation and control of martensite in Ti-6Al-4V alloy produced by selective laser melting. *Mater Des* 108:308–318

**Publisher's note** Springer Nature remains neutral with regard to jurisdictional claims in published maps and institutional affiliations.